Earth, Planets and Space

FULL PAPER

Contribution of microtopography off the Ryukyu Islands to coastal sea-level amplification during the 2022 Tonga meteotsunami

Takuya Miyashita[1*], Ai Nishino[2], Shingo Watanabe[3], Tomohiro Yasuda[4], Nobuhito Mori[1,5], Tomoya Shimura[1] and Tung-Cheng Ho[6]

Abstract

The January 2022 Tonga volcanic eruption generated atmospheric pressure waves that propagated over the ocean's surface and triggered a meteotsunami. This meteotsunami caused significant amplitudes exceeding 100 cm along various Pacific coastlines far from the volcano. However, the factors driving such amplification remain unclear. This study presents numerical simulations of the meteotsunami, focusing on the Ryukyu Islands in Japan, where a maximum amplitude of 100 cm was recorded. Two models for simulating pressure waves from the eruption were utilized: one based on the superposition of waves tuned using the dispersion relation of atmospheric gravity waves (synthetic waves), and the other based on a detailed numerical model that assumes the release of a heat source from the eruption vent. The synthetic pressure wave simulations showed good agreement with the observations, accurately reproducing the 100 cm amplitude at Amami. To further analyze the factors contributing to the large amplitude at Amami, additional simulations were conducted by limiting the resolution to offshore areas deeper than 2000 m while maintaining a high resolution in coastal bathymetry. These simulations showed that reducing offshore resolution decreased the amplitude at Amami from approximately 100 to 60 cm, highlighting the significant role of offshore microtopography such as Daito Ridge and Oki-Daito Ridge in coastal amplification. The difference in amplitude was particularly notable in ridge areas with depths of 2000–5000 m. Moreover, the proportion of free waves to the total tsunami amplitude was estimated by terminating atmospheric pressure forcing during the computation. The results indicated that free waves alone could amplify from less than 5 cm offshore to 50 cm at the Amami coast, which is approximately half the amplitude when forced waves are also considered. These findings provide crucial insights into assessing the future predictability of meteotsunamis. Future research should investigate the necessary resolution and relationship between atmospheric wave properties and tsunami amplification. Understanding these factors is essential to improve the prediction and risk assessment of meteotsunamis.

Keywords 2022 Hunga Tonga–Hunga Ha'apai eruption and tsunami, Meteotsunami, Oceanic ridge, Offshore topography, Bathymetry

*Correspondence:
Takuya Miyashita
miyashita.takuya.4w@kyoto-u.ac.jp
Full list of author information is available at the end of the article

Graphical Abstract

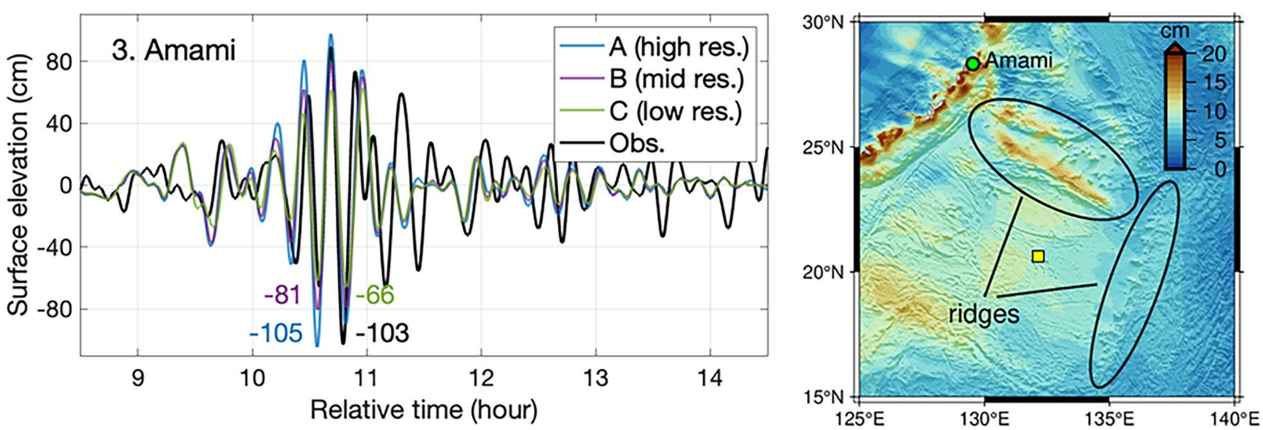

1 Introduction

In January 2022, a massive eruption of the Hunga Tonga–Hunga Ha'apai volcano in the Kingdom of Tonga generated atmospheric pressure waves, resulting in various types of pressure waves being observed worldwide (Matoza et al. 2022; Shinbori et al. 2023; Horvath et al. 2024). These atmospheric pressure waves excited the sea surface, and the excitation continued to increase as the waves traveled. This phenomenon is referred to as a meteorological tsunami (meteotsunami). Typical meteotsunamis are caused by atmospheric disturbances (Monserrat et al. 2006; Rabinovich 2020). This Tonga meteotsunami was unique in that the atmospheric pressure waves were caused by a volcanic eruption, which is a rare occurrence. The last confirmed volcanic meteotsunami before this event was generated by the 1883 Krakatoa eruption (Nomanbhoy and Satake 1995). After the volcanic eruption in Tonga, oscillations at sea level that could be identified as meteotsunamis were observed on coasts worldwide. The occurrence of these meteotsunamis was not only limited to the South Pacific but was also confirmed in the Caribbean and Mediterranean seas (Devlin et al. 2023; Heinrich et al. 2023).

The area affected by the tsunami caused by the collapse of the caldera from this eruption was relatively small. However, meteotsunamis exceeding 1 m in height have been observed on the coasts of Chile, the United States, and Japan, which are more than 8000 km away (e.g., Carvajal et al. 2022; Takahashi et al. 2023; Pacheco et al. 2024; Imamura et al. 2022; Lynett et al. 2022). As indicated in previous studies, the amplification factor of these meteotsunamis is attributed to Proudman resonance. Proudman resonance is a phenomenon in which forced waves are gradually amplified when the wave speed of the sea surface and the propagation speed of atmospheric disturbances are roughly equal. The 2022 Tonga eruption generated Lamb waves that travel at the speed of sound, Pekeris waves associated with the internal mode of atmospheric free oscillation, and atmospheric gravity waves of various wavelengths and speeds (Wright et al. 2022; Watanabe et al. 2022). The impact of each of these atmospheric waves on sea surface excitation has been studied previously.

The sea-surface excitation caused by the Lamb wave, which had the largest pressure amplitude and was the first to reach Japan, has been extensively studied (e.g., Kubota et al. 2022; Yamada et al. 2022). These studies have shown that the behavior of the meteotsunami during the first 1 to 2 h can be largely explained by the excitation from the Lamb wave offshore and wave shoaling. Regarding the Pekeris wave, Watanabe et al. (2022) reproduced the generation of this wave from the eruption using climate simulations. Subsequently, Suzuki et al. (2023) conducted meteotsunami simulations based on the simulated Pekeris wave, demonstrating that the Pekeris wave played an important role in forming part of the meteotsunami observed in Japan. For atmospheric gravity waves, individual waves with various wavelengths propagated at different speeds and reached Japan. Several studies shown that these waves significantly contributed to the generation of subsequent waves several hours after the arrival of the Lamb wave (e.g., Nishikawa et al. 2022; Miyashita et al. 2023). These waves propagate at their respective inherent speeds; however, because the speed of ocean long waves is determined by water depth, in areas with significant changes in water depth, forced waves cease to exist and transform into free waves.

A representative amplification mechanism for free waves is bay resonance. Bay resonance occurs when the period of the incident waves entering from the mouth of the bay coincides with the natural period of the bay, causing the wave phases to overlap and amplify. It has been suggested that the Tonga meteotsunami may have experienced amplification owing to bay resonance (Pakoksung et al. 2023; Zaytsev et al. 2024). However, in some locations, these two amplification mechanisms alone cannot explain the amplitudes exceeding 1 m. Even when meteotsunamis are simulated with sufficient horizontal resolution to capture the bay resonance, pressure waves with amplitudes less than 1 hPa cannot reproduce the observed amplified waves (Miyashita et al. 2023). Therefore, to understand the amplification of this meteotsunami, it is necessary to focus on amplification phenomena other than Proudman and bay resonances.

To understand the amplification, it is essential to use offshore and coastal observational data. Observations from the Deep-Ocean Assessment and Reporting of Tsunamis (DART) buoys indicate that, in the deep ocean of the northwest Pacific, sufficiently distant from the volcano, the maximum amplitude is approximately 5 cm. Therefore, the influence of Proudman resonance at these locations was minimal. In contrast, the tide gauges on the coast of Amami Island, approximately 900 km away from the nearest DART 52404, recorded amplitudes exceeding 100 cm. This indicates that amplification from 5 to 100 cm occurred over the distance between the deep ocean and shallow coast. Similar amplifications of up to 100 cm were recorded along the coasts of North and South America (Omira et al. 2022; Zaytsev et al. 2024). However, the primary factors contributing to these amplifications and the magnitude of each factor contribution have not yet been quantified. Understanding the amplification mechanisms is crucial not only for volcanic meteotsunamis but also for evaluating the predictability of meteotsunamis caused by general atmospheric disturbances.

This study aims to reproduce the significant tsunami amplitudes observed in the Ryukyu Islands, including the Amami Islands in Japan, during the 2022 Tonga meteotsunami and to understand the amplification factors from offshore to coastal areas. Specifically, we focused on Amami, which is one of the locations that recorded the largest amplitudes along the Japanese coast. Eastern Japan has a dense offshore observation network that has enabled extensive analysis of this meteotsunami (e.g., Kubo et al. 2022; Tanioka et al. 2022; Wang et al. 2023). However, in southwestern Japan, including the Ryukyu Islands, such offshore observations are sparse, leaving many aspects of the amplification process unexplained. The main methodology of this study is similar to that of a previous work (Miyashita et al. 2023), but focuses on these unexplained areas and provides a more detailed analysis. In addition, this study quantified the contribution of the representation of microtopography in deep-ocean areas to meteotsunami amplitudes.

The remainder of this paper is organized as follows. First, the next section provides an overview and description of the meteorological and oceanographic data, along with an explanation of the numerical computation methods. Subsequently, the numerical results of the meteotsunami simulated under various meteorological conditions were compared with observational data to validate the differences in reproducibility. Based on this comparison, the major factors contributing to significant tsunami amplification at the Amami location were estimated. Furthermore, additional simulations were performed considering the conditions of the numerical simulations that successfully reproduced the amplification. The spatial distribution of the amplification mechanisms and their physical processes are discussed. The final section presents conclusions.

2 Data and methods

2.1 Observation data acquisition

To understand the physical phenomena and compare and validate the simulation results, this study used observational sea surface pressure and sea level data. Observations from the Japan Meteorological Agency (JMA) were used for pressure data. JMA conducts observations across all the land areas in Japan. The observation results indicate that, near Japan, the pressure waves generated by this eruption were initially characterized by Lamb waves with an amplitude of approximately 2 hPa passing at nearly the speed of sound, followed by small atmospheric gravity waves with amplitudes of less than 0.5 hPa arriving over the subsequent hours. To validate the pressure data used in the tsunami simulations described later, time series are compared at two locations where the effects of topographic shielding are expected to be minimal.

Two types of sea level data were used in this study. One was from the DART instruments managed by the National Oceanic and Atmospheric Administration (NOAA). These instruments are widely deployed across the world's oceans and cover deep-ocean areas. Thus, they are useful for capturing the amplitude changes from the deep ocean to shallow coastal areas. Six specific recordings located between the volcano and the Japanese coast were used among the waveforms recorded by the DART buoys across the Pacific. The positions and numbers of stations are shown in Fig. 1a. NOAA provides the data in the form of sea level anomalies by applying a filter (Mungov et al. 2013), which were used in this study. However, note that the DART stations record bottom

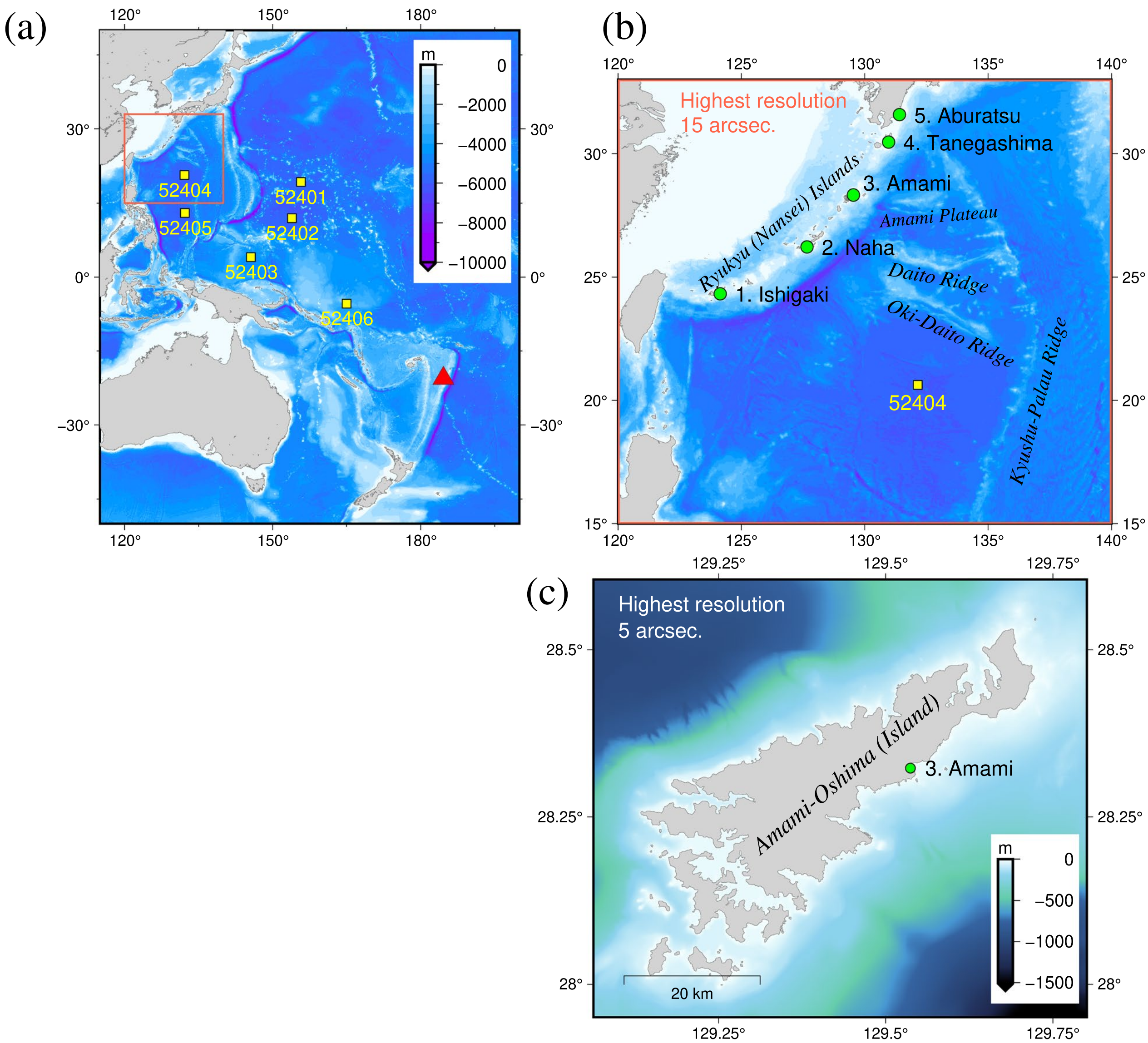

Fig. 1 Bathymetry distributions conditioned for the tsunami simulation. The red triangle represents the location of the volcano, and numbered yellow boxes represent DART buoys. **a** Full simulation domain; **b** enlarged view of southwest Japan, including the Ryukyu islands areas; and **c** coastal area around Amami Island

pressures and these data originally include atmospheric pressure changes. Complete separation of the oceanic pressure changes from the atmospheric pressure changes is difficult. Hence, the unit cmH_2O is considered more appropriate for describing the DART data in this study.

The other type of sea level data comes from coastal gauges, which are managed by JMA and are installed widely along the Japanese coast. During the meteotsunami event, these gauges recorded tsunamis across the country. In this study, five locations in the southwestern islands of Japan were selected, as shown in Table 1, and are used to validate the coastal

Table 1 Properties of JMA tidal gauges and maximum amplitudes

Number	Name	Latitude (°N)	Longitude (°E)	Max. amplitude (cm)
1.	Ishigaki	24.33	124.16	17
2.	Naha	26.21	127.67	29
3.	Amami	28.32	129.53	103
4.	Tanegashima	30.46	130.96	50
5.	Aburatsu	31.58	131.41	66

tsunami amplitudes. Table 1 also lists the maximum amplitudes observed during this meteotsunami event, ranging from locations with amplitudes of less than 20 cm (1. Ishigaki) and those exceeding 100 cm (3. Amami). Detailed locations of the coastal gauges are shown in Fig. 1b. Both the atmospheric pressure and sea level data were processed to remove long-period components and extract the pressure and sea-surface anomalies for comparison with the simulation results.

Two types of datasets were used for bathymetry data. The General Bathymetric Chart of Oceans (GEBCO) Dataset 2023 was used for broad areas. GEBCO is a bathymetry dataset with a resolution of 15 arcseconds that covers the entire globe, encompassing the entire region of tsunami simulations (Fig. 1a). The other dataset comprised bathymetry and topography data published by the Central Disaster Management Council of the Japanese Cabinet Office. This dataset was used particularly for reproducing the amplification of tsunamis in coastal areas with a resolution of 5 arcseconds. This resolution corresponds to approximately 150 m around Amami Island, which is sufficient to capture the geometry necessary for reproducing the bay resonance. The data originally provided in the plane rectangular coordinate system were converted to latitude and longitude data using the Gauss–Krüger projection method Kawase (2013). As described later, the spatial and temporal resolutions during tsunami simulations can vary with the computation time. However, the highest resolution during the simulations depended on the available data, with 15 arcseconds for offshore areas and 5 arcseconds for shallow sea areas around Amami Island.

Figure 1b illustrates the bathymetry of the Ryukyu Islands. Several ridges lie in the southeast offshore of the five JMA gauges, which are marked in green circles. The Kyushu-Palau Ridge extends north–south offshore from 5. Aburatsu station. Oki-Daito Ridge and Daito Ridge are located offshore, 2. Naha station. Amami Plateau is located off the coast of 3. Amami station. Between these ridges and the coast lies a deep region with depths ranging from 6000 to 7800 m, known as the Ryukyu Trench. The bathymetry around the Ryukyu Islands is characterized by a series of ridges and trenches, which are expected to play a significant role in the amplification of meteotsunamis.

2.2 Pressure wave generation/simulation

Tsunami simulations require the spatiotemporal distribution of the surface atmospheric pressure. In this study, two types of spatiotemporal pressure distributions were created. The differences between the two methods are shown in Fig. 2. One dataset was synthesized using the dispersion relationship of atmospheric gravity waves to create simple waves. This method and dataset are identical to those used by Miyashita et al. (2023). For further details, refer to their work. The linearized dispersion relation of atmospheric gravity waves is expressed as follows:

$$\omega^2 = \frac{c_s^2}{2}\left(k^2 + m^2 + \mu^2\right)\left[1 - \sqrt{1 - \frac{4k^2N^2}{c_s^2\left(k^2 + m^2 + \mu^2\right)}}\right], \quad (1)$$

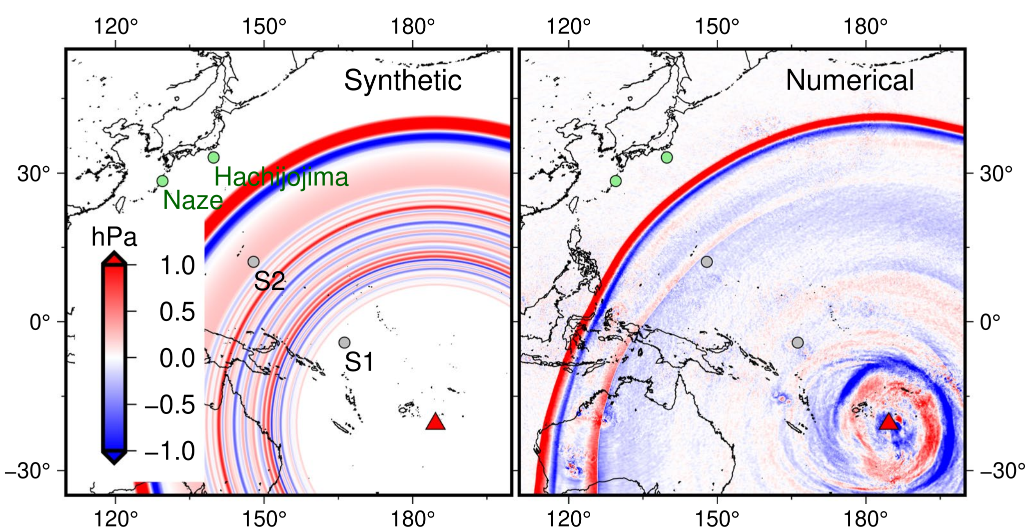

Fig. 2 Snapshots of the spatial distribution of air pressure field. The left panel shows the sea level pressure anomaly generated by the combination of tuned amplitudes and the dispersion relation. The right panel shows that of numerically simulated data by JAGUAR. The red triangle in the South Pacific represents the volcano. The green circles indicate the JMA pressure gauge, and the gray circles labeled S1 and S2 indicate the station virtuality located for comparison

$$\mu = \frac{1}{2}\left(\frac{N^2}{g} + \frac{g}{c_s^2}\right), \quad (2)$$

where ω is the angular frequency, c_s is the speed of sound, k and m are wavenumbers in the horizontal and vertical directions, respectively, N is the buoyancy frequency, and g is the gravitational acceleration. Using this equation, the unique period and wave speed can be determined for a given gravity wave wavelength. Assuming that waves of different wavelengths radiate from the same point source simultaneously and evolve over time, a horizontal spatial pattern is generated as each wave propagates at a different speed. Various spatial patterns of sea surface pressure can be created using different wavelengths and their corresponding amplitude parameters. By tuning the combinations of wavelengths and parameters, spatiotemporal distribution data were created to match the time series of atmospheric pressure observations in Japan. The temporal interval of data was 1 min. During the numerical simulations, the spatial distribution of the pressure between the 1-min intervals was interpolated. It should be noted that gravity waves cannot be generated without considering the thermosphere (Tonegawa and Fukao 2022); thus, this simplified assumption is limited in its representation of actual gravity waves. The horizontal resolution of the pressure data was 6 arcminutes (~ 10 km).

The other pressure distribution was a pressure anomaly simulated using a numerical model. The Japanese Atmospheric General circulation model for Upper Atmosphere Research (JAGUAR; Watanabe and Miyahara 2009) is used to simulate the generation and propagation of atmospheric Lamb, Pekeris, and gravity waves resulting from the Tonga volcanic eruption. The details of this data are described in Watanabe et al. (2022). Unlike the synthesized waves mentioned earlier, this model considers the realistic atmospheric wind and temperature profile up to the lower thermosphere. This consideration allows for the solution of a more complex three-dimensional wave propagation. It is important to note that this simulation aims to reproduce Lamb and Pekeris waves and does not specifically aim to reproduce the spatiotemporal distribution of subsequent trailing gravity waves around Japan. However, comparing tsunami simulations using the conditions of this simulated wave with those using the synthetic wave allows the investigation of the impact of pressure waves on meteotsunamis, which cannot be reproduced by simplified assumptions. Although the simulations were conducted in three dimensions, only the pressure at the sea surface level was extracted for use in the tsunami simulations. The interaction between the atmosphere and the ocean was not considered in the JAGUAR model. The temporal interval of distribution was 1 min. The horizontal resolution of the pressure data was 3 arcminutes (~ 5 km), which is higher than that of the synthetic data.

Figure 2 simultaneously shows the spatial distribution of the surface pressure anomalies at the same time for the two types of pressure data. The synthetic pressure assumes a uniform spatial pattern, resulting in a simple superposition of spatial patterns. In contrast, the pressure simulated by JAGUAR exhibited an anisotropic spatial pattern. Only one of the following waves is prominently displayed; this subsequent wave corresponds to the Pekeris wave.

Figure 3 presents a comparison of the waveforms and wavelet analyses at several locations. The positions of these locations are shown in Fig. 2. In this study, the passage of time was represented using relative time based on the main eruption time. Two of the four locations are JMA meteorological observation sites, while the remaining two are virtual gauge stations that approximately evenly divide the area between the volcano and the Ryukyu Islands of Japan. No observational data were available for these stations. At the location closest to the volcano, the passage of the pressure waves was concentrated within a short time. As the distance from the volcano increases, the components of each wave separate owing to differences in wave speed. The observational waveforms contain the most diverse components, including noise. Synthetic waves also show the separation of waves as they approach Japan. As they were tuned, the waveforms represented the observational waveforms well. The pressure waves from the JAGUAR model primarily exhibited an initial Lamb wave and a subsequent Pekeris wave, with few of the other components observed in the actual data.

2.3 Numerical tsunami simulation

Numerical simulations of the meteotsunami were conducted using the spatiotemporal distribution of the surface atmospheric pressure as the forcing condition. The GeoClaw package (Mandli and Dawson 2014) was used for the meteotsunami simulations. This model is based on nonlinear shallow water equations commonly used for tsunami and storm surge simulations and was solved using the finite volume method. The model employs an adaptive mesh refinement (AMR) method, which allows it to change the time interval and spatial resolution as required during its computation. Specifically, when tsunami waves have not yet arrived or are negligible, the simulation is performed with coarse time intervals and spatial resolutions. This capability makes the model useful for wide-area tsunami simulations, such as the Tonga meteotsunami event (Omira et al. 2022; Yuen et al. 2022). As mentioned in the

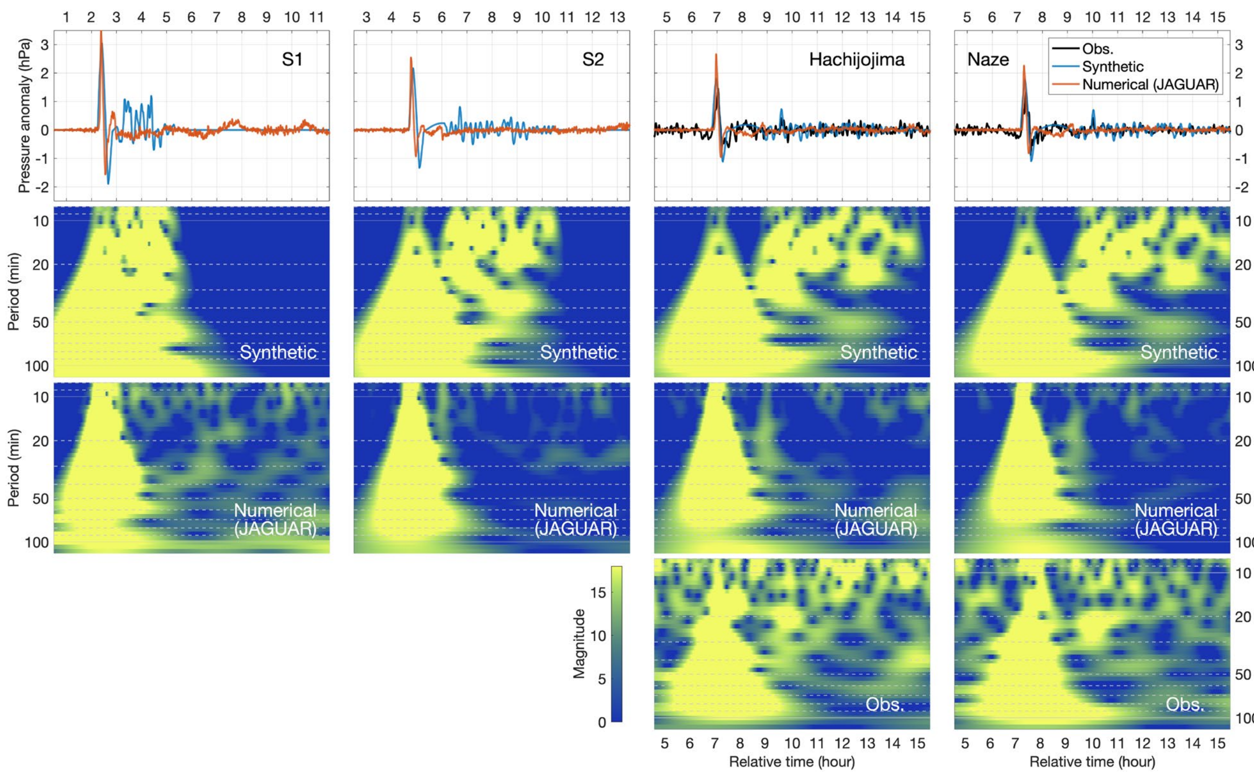

Fig. 3 Pressure waveforms and wavelet analysis at 4 pressure gauges. The top four panels show the comparisons of time-series sea level pressures. The horizontal axis represents the relative time based on the main eruption time. The other panels show the wavelet (*f-t*) diagrams for the observed data and synthetic pressure model and numerical model JAGUAR, respectively

bathymetric data description, the entire computational domain was covered by GEBCO2023 data with a resolution of 15 arcseconds. However, only the shallow coastal area around Amami Island used the 5 arcseconds data from the Cabinet Office. Thus, the highest resolutions for most regions were 15 arcseconds and 5 arcseconds only around Amami Island. However, using these resolutions uniformly across all regions at all times is computationally infeasible. Therefore, five resolution levels were utilized: 12 arcminutes, 4 arcminutes, 1 arcminute, 15 arcseconds, and 5 arcseconds, from coarsest to finest. The highest resolution was achieved only when the tsunami amplitude was sufficiently large in the surrounding area. To accurately represent the offshore topography and bathymetry of southwestern Japan, a specific region was designated for computation at 15 arcseconds even offshore.

The computational domain is shown in Fig. 1a, and the region computed in detail at 15 arcseconds is shown in Fig. 1b. Figure 1c shows the region around Amami at a resolution of 5 arcseconds. The time increment of the simulation was automatically determined to ensure that the (Courant–Friedrichs–Lewy) CFL number remained sufficiently small according to the resolution level. Astronomical tides were not considered, and the initial water level was set to zero throughout the domain. The configuration files for the simulations are publicly available, and anyone can replicate the calculations. For more details, refer to available data and materials.

3 Results

First, we compared the simulated results with the observed tsunami waveforms. Figure 4 compares the waveforms from the DART buoys in deep-ocean regions. For the observational data, continuous oscillations lasting several hours or more were observed at all locations from the onset of the initial water level change. However, the amplitudes were less than 5 cm. The initial excitation by the Lamb wave was in good agreement in both simulations using synthetic pressure and simulated (JAGUAR) pressure conditions. At station 52406, which was the closest to the volcano among the six stations, the simulated amplitude was smaller than the observed amplitude. This discrepancy may have occurred because the atmospheric pressures were tuned to match the pressure anomalies near Japan, making it likely that the pressure amplitudes at locations far from Japan would differ from the actual values. In addition, the short period

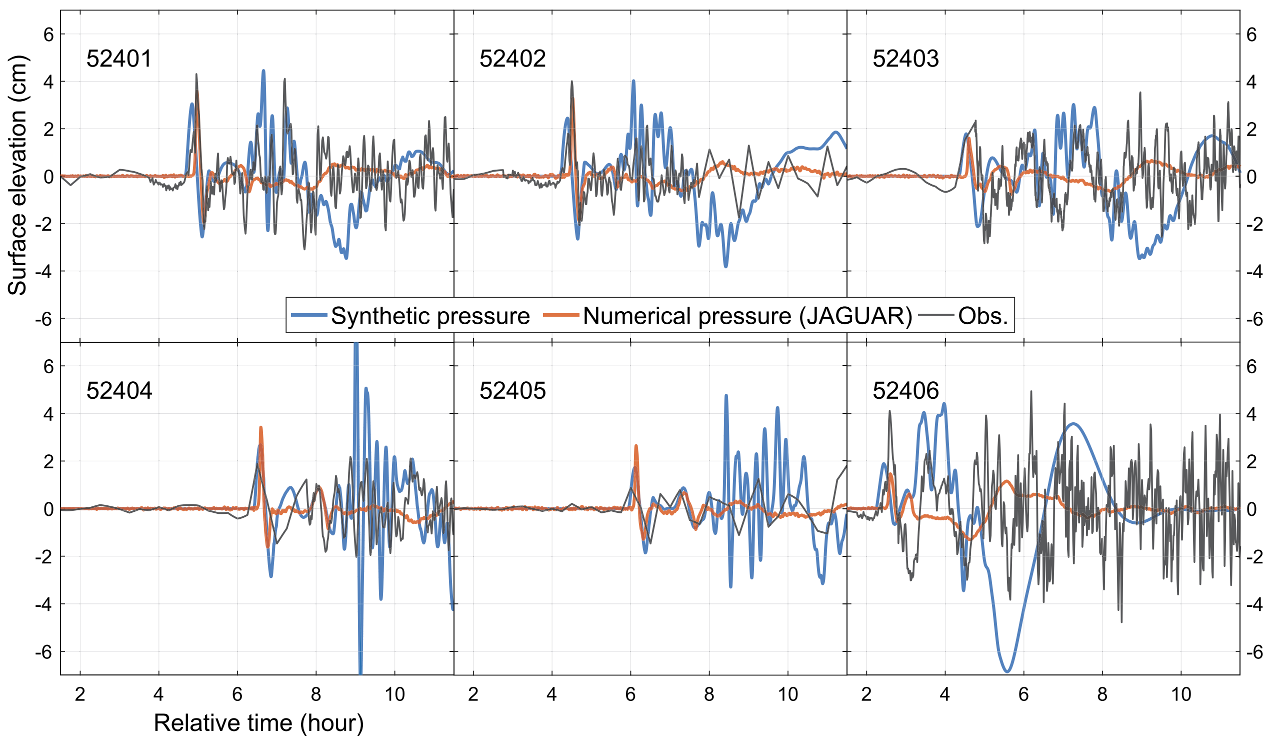

Fig. 4 Comparison of simulated and observed tsunami waveforms for the six DART gauges. Blue, orange, and black lines represent the simulated waveforms under the synthetic pressure and JAGUAR pressure, and the observed waveforms, respectively. The relative time on horizontal axes is based on the main eruption time

components of the DART data were filtered out, which may have caused the discrepancy in the amplitude.

At station 52404, the closest to the Ryukyu Islands, the tsunami amplitudes simulated under the synthetic pressure condition (~7 cm) exceed the observed amplitudes (~2 cm) during the period following the arrival of the Lamb wave. This discrepancy is likely due to the synthetic pressure being slightly larger than the observed pressure. In particular, the synthetic pressure exhibits stronger short-period components compared to observations, as shown in the comparison at the Naze location in Fig. 3. Consequently, this may result in a slight overestimation in the subsequent comparisons for coastal regions. However, overall, the tsunami amplitudes at the DART stations under the synthetic pressure condition were generally close to the observed amplitudes. In contrast, under the JAGUAR condition, the oscillations following the Lamb wave excitation are smaller, and there are weaker high-frequency components. As shown in Fig. 3, the pressure anomalies from JAGUAR include only the components of the Lamb wave and gravity waves within specific frequency bands.

Figure 5 shows a comparison between the observed and simulated tsunami waveforms at JMA coastal gauges. While the difference in tsunami amplitudes between the synthetic and JAGUAR conditions was only a few centimeters offshore, as observed with DART, this difference significantly increased in coastal areas. Under synthetic pressure conditions, the simulated tsunami waveforms closely matched the observed waveforms at the five locations. The maximum amplitude ranged from approximately 20 cm (1. Ishigaki and 2. Naha) to 100 cm (3. Amami), which is in good agreement with the observations. However, prolonged oscillations were observed 12–15 h after the eruption at 4. Tanegashima and 5. Aburatsu, that were not reproduced accurately. This limitation is likely due to the representation of pressure waves through the superposition of a finite number of waves. In contrast, the tsunami waveforms under the JAGUAR condition show similar patterns to the synthetic conditions for the first few hours after the initial water level excitation but do not exhibit significant subsequent amplifications. This was because the pressure amplitudes after the passage of the Lamb wave were smaller. In addition, these results indicate that pressure waves that cannot be expressed without considering the vertical structure of the atmosphere are not the main contributors to the significant tsunami amplification observed along the coast.

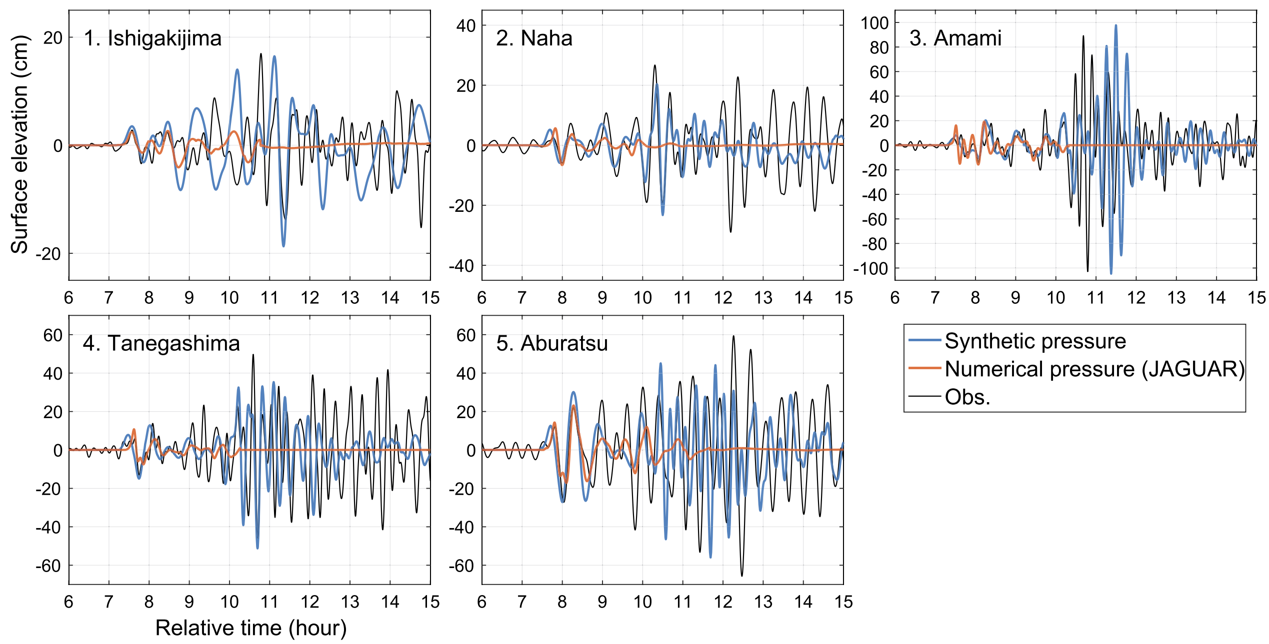

Fig. 5 Comparison between simulated and observed tsunami waveforms at coastal gauges. The line colors are similar to that in Fig. 4

While the simulated waveform at Amami generally shows good agreement with observations, the simulation failed to match the occurrence time of the maximum amplitude. This discrepancy is likely due to the assumptions of linear theory and constant wave speed in the synthetic wave model. The Lamb wave was constructed based on the observed signal, which exhibited a clear speed, allowing for accurate modeling. However, for atmospheric gravity waves, it is not possible to determine individual wave speeds and periods directly from observations. Furthermore, the dispersion relation of atmospheric gravity waves depends on parameters such as temperature and adiabatic lapse rate, which are spatially non-uniform. In this study, the synthetic waves assumed these parameters to be uniform across the entire domain, potentially introducing discrepancies in the dispersion relation compared to reality. The influence of wind during propagation also cannot be neglected as a factor contributing to the timing mismatch.

This study successfully reproduced the maximum amplitude at Amami station, which recorded the largest amplitude among the JMA gauges. However, our previous work (Miyashita et al. 2023) could not show such a result despite the use of the same synthetic pressure data. The difference in the conditions between the two studies was the resolution of the offshore bathymetry. In the previous study, to perform simulations for the entire Japanese coasts, deep-depth areas were coarsely represented due to computational limitations. In contrast, this study focused on Ryukyu Islands, and the offshore bathymetry was represented at a higher resolution. This difference was considered to have a significant impact on the tsunami amplification. In the next section, we will further investigate the impact of the offshore bathymetry resolution on the tsunami amplification.

4 Assessment of the amplification factors

To further clarify the cause of the amplification up to 100 cm at Amami station, numerical experiments focusing on the representation of offshore microtopography were conducted. Figure 6 illustrates the differences in the AMR criteria region specifications. In this experiment, three regions, designated as Regions A, B, and C, were set up, as shown in the figure, and three types of simulations were performed for each region. These regions indicate the range within which computations can be performed at the highest available resolution of 15 arcseconds. Thus, outside these regions, even if the tsunami amplitude is sufficiently large, the AMR resolution level is restricted, and the computations are performed at the next lower resolution level, namely, 1 arcminute. The only difference in the computation conditions pertains to these regions, whereas the pressure anomalies use synthetic data.

Region A was identical to the synthetic pressure condition simulation mentioned above and covered the same area as that shown in Fig. 1b. Region A includes the Kyushu-Palau Ridge running north–south near longitude 135° E and two east–west ridges slightly further west (Daito Ridge and Oki-Daito Ridge from north to

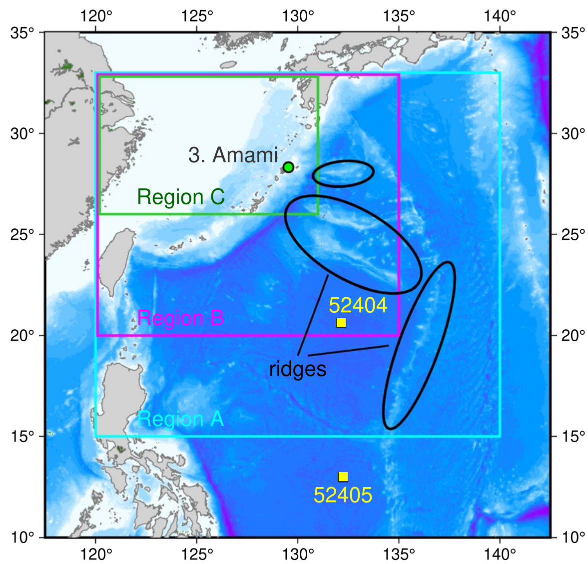

Fig. 6 Numerical configuration of different resolution domains for comparison. The labeled frames indicate regions where the highest resolution of 15 arcseconds is achieved during the AMR simulations. Region A is the same size as Fig. 1b, and the area of the regions decreases as they move from A to B and then to C. Outside these regions, the highest resolution used is one level lower, at 1 arcminute

south). In contrast, Region B does not include most of the Kyushu-Palau Ridge but consists of the remaining Daito Ridge group. This means that the detailed topography of the Kyushu-Palau Ridge was not represented in the tsunami simulations. Region C does not include any of these ridges. As we moved from Region A to Region C, the area computed at the highest resolution of 15 arcseconds becomes smaller. The summits of these ridges are approximately 2000–3000 m deep, while the surrounding depths at the bases of the ridges are approximately 5000–6000 m. This study evaluates the impact of differences in the representation of offshore bathymetry centered around these ridges on the amplification of meteotsunamis.

Figure 7 compares the tsunami waveforms at Amami resulting from the meteotsunami simulations performed under the configurations of Regions A, B, and C. Note that the waveforms for Regions A, B, and C were time offset to facilitate comparison with the observed waveform. Focusing on the right panel of the figure, it is evident that the wavelet components of the tsunami waveforms were almost identical across Cases A, B, and C because of the use of the same pressure data, with only slight differences in intensity. However, the maximum amplitudes differed significantly: 105, 81, and 66 cm for Cases A, B, and C, respectively. This substantial difference in the maximum amplitude of approximately 40 cm on the Amami coast arises solely from changing

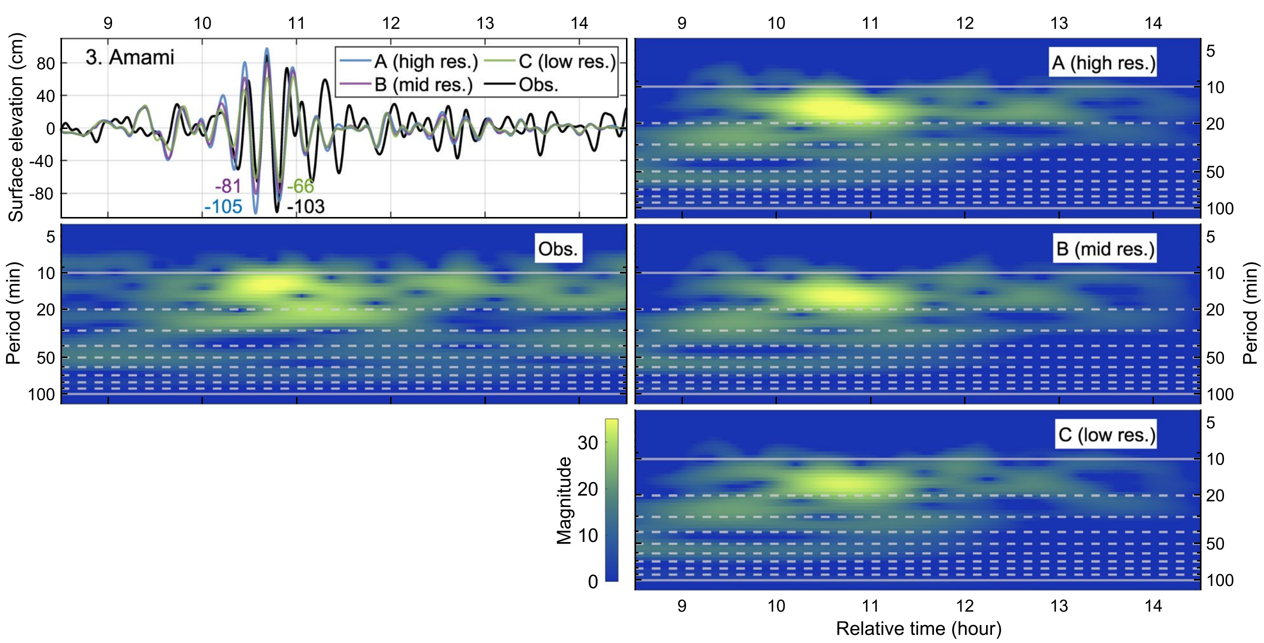

Fig. 7 Comparison of tsunami waveforms and scalograms at the Amami station between different horizontal resolution simulations with Regions A, B, and C. The top left panel shows the waveform comparison. The black line represents the observed waveform and the other lines represent the simulated waveform using Regions A (blue), B (purple), and C (green). The middle left and right panels show the observed and simulated scalograms. Note that the waveforms for Regions A, B, and C were time offset for the comparison with the observed waveform

the region of high-resolution computation offshore, even though the coastal area is computed at 5 arcseconds resolution. The predominant periods between 10 and 20 min observed in the wavelet analysis of the computed waveforms were also present in the observed waveforms, suggesting the occurrence of bay resonance. This indicates that while the bay itself is sufficiently well-represented at high resolution, offshore bathymetry plays a significant role in the accurate reproduction of tsunami amplification.

Next, we focused on the spatial distribution of the maximum tsunami amplitudes. Figure 8 shows the spatial distribution of the maximum amplitudes around Amami Island for Cases A to C. The spatial pattern of the maximum amplitudes around Amami Island was generally the same in the simulations of Cases A and C. In all bays facing the southeast direction, where the pressure waves originate, the amplitudes significantly increase toward the inner parts of the bays, indicating the occurrence of resonance. Amami Station is one of the bays in which resonance occurs. Even in Case C, there were no changes in the spatial characteristics compared with Case A, and resonance was also considered to have occurred. Therefore, the maximum amplitude difference of 40 cm at the Amami station between Cases A and C is likely due to the intensity of the tsunami waves incident offshore of the Amami Island area.

Figure 9 compares the spatial distribution of the maximum amplitudes in the region encompassing Amami and the offshore ridges between 125° E and 140° E and 15° N and 30° N. The upper panels show the amplitudes, whereas the lower panels show the differences compared to Case C. In all the cases, the amplitudes were larger in the ridge areas than in the surrounding regions. However, the magnitude of amplification varied between cases. Notably, in the lower panels in Fig. 9, the difference in wave amplitude increases as the waves cross the ridges. The amplitude difference between Cases A and C (bottom left) was approximately 8 cm near Daito Ridge, and this amplification effect further increased as the waves moved from the ridge area toward the coast. Additionally, the differences in shallow coastal areas became more pronounced as waves entered the bays around Amami. The incident wave amplitudes differed between cases A and C, and as these waves triggered bay resonance, a significant difference of up to 40 cm in amplitude was observed along the coast.

Based on the above results, the significant amplification observed in the Ryukyu Islands, particularly in Amami, during the 2022 Tonga meteotsunami was successfully reproduced by our simulations. The simulated maximum

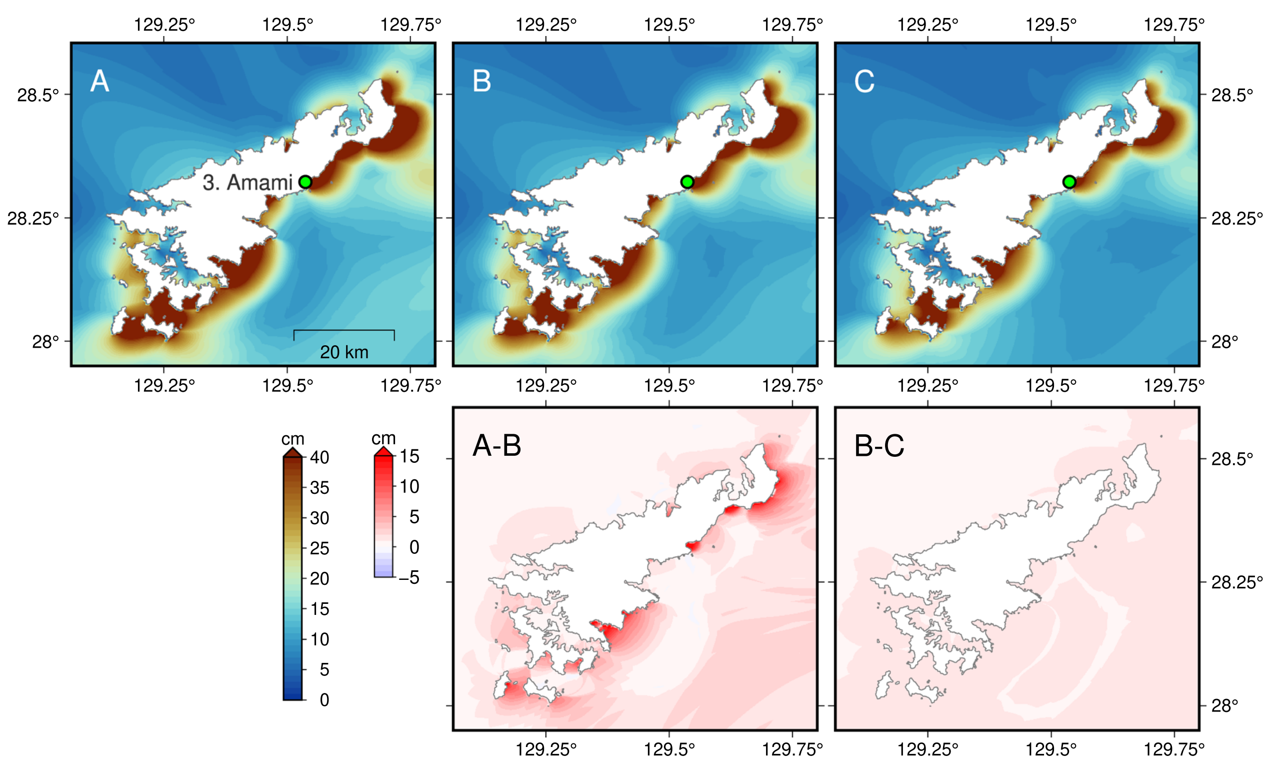

Fig. 8 Spatial distributions of maximum tsunami amplitude around Amami Island for the simulation with Regions A (left), B (middle), and C (right). The lower panels show the difference between the maximum amplitudes of A to B and B to C, respectively

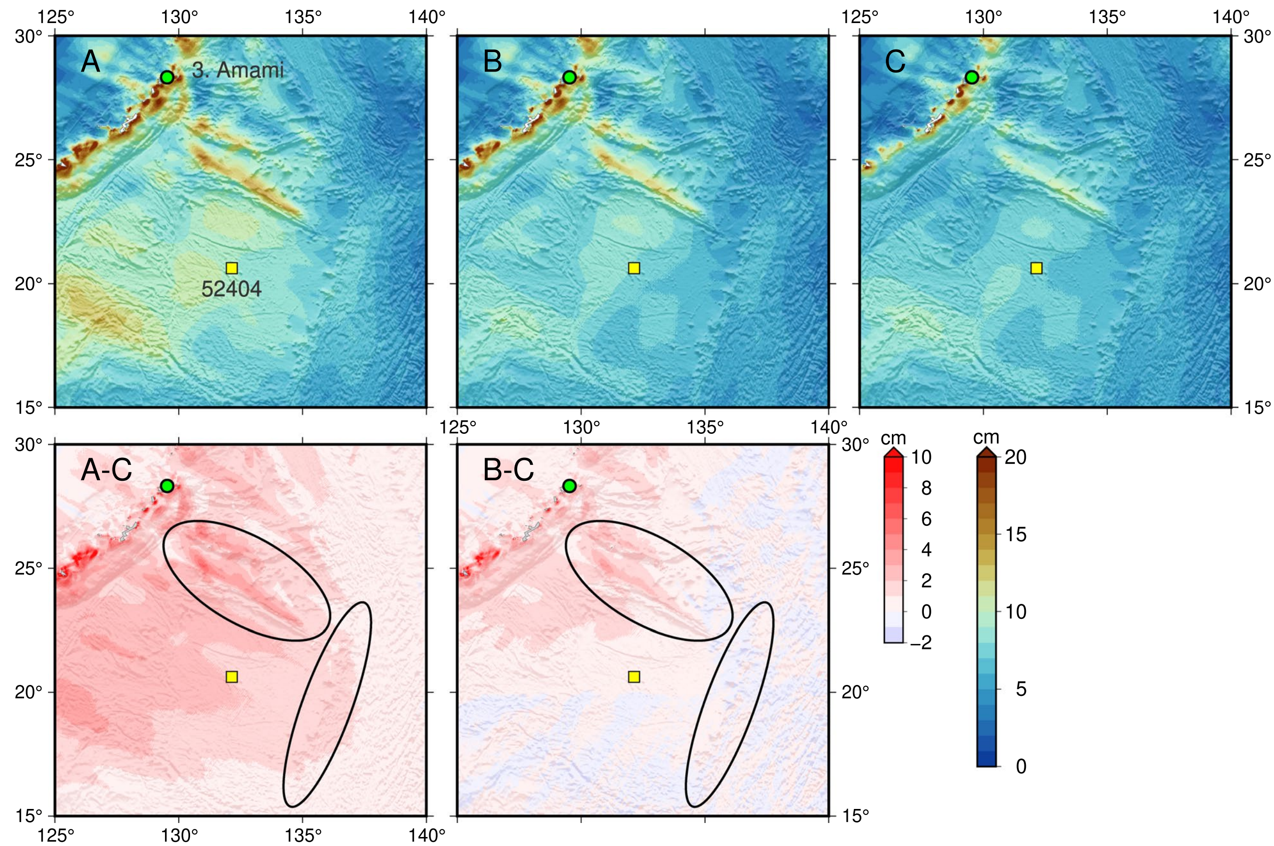

Fig. 9 Comparison of maximum tsunami amplitude between different resolution configurations off the Ryukyu Islands. The top panels show the spatial distributions of the maximum tsunami amplitude, and the bottom panels show the difference from Case C. Black ellipses represent the locations of Kyushu-Palau Ridge and Daito Ridges

amplitudes were generally in good agreement with the observations. This study indicated that to achieve results consistent with observations, the numerical simulation requires consideration of microtopography in the deep sea and not just high-resolution computations in coastal areas. Specifically, the wave amplitude increased significantly before and after passing over ridges with summit depths of 2000–3000 m, which likely contributed to the substantial amplification observed at Amami. Furthermore, under simulation conditions that closely matched observations, the amplitude gradually increased offshore from the Ryukyu Islands, even outside the ridge areas. This can be caused by the continuous excitation of the sea surface due to horizontal pressure gradients, such as those represented by Proudman resonance.

The results above showed the spatial resolution offshore from the Ryukyu Islands can significantly alter the overall tsunami amplitude. Changes in resolution during the tsunami simulation alter the representation of not only bathymetry but also atmospheric pressure. Therefore, the differences between the cases of the refinement regions might be attributed solely to the resolution of the pressure data rather than the offshore bathymetry. To confirm this, the input resolution of the synthetic pressure was deliberately coarsened, and the computation was performed under the conditions in Region A.

Figure 10 shows the tsunami waveforms at 3. Amami under the conditions of the synthetic pressure with different resolutions. The blue line represents the result of the original simulation (identical to the blue line in Fig. 7), which used a resolution of 6 arcminutes for the atmospheric pressure. The yellow and red lines represent the results of the simulations with resolutions of 15 arcminutes and 30 arcminutes, respectively. The only difference between these simulations was the resolution of the atmospheric pressure data. The waveforms were almost identical in the initial phase, but the amplitudes differed only around the maximum amplitude. The result of 15 arcminutes resolution was very close to the original result, whereas the result of 30 arcminutes resolution was significantly different. The difference in the maximum amplitude between the 6 arcminutes and 15 arcminutes resolutions was 5 cm: 105 cm and 100 cm, respectively. Additionally, the 15 arcminutes resolution

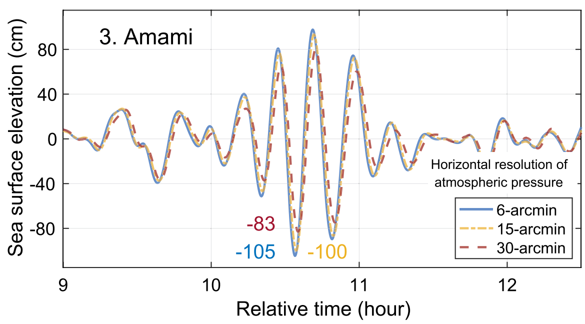

Fig. 10 Comparison of tsunami waveforms at the Amami station between different resolutions of atmospheric pressure. The blue line is identical to that in Fig. 7, representing the case of Region A. Its horizontal resolution of atmospheric pressure is 6 arcminutes. The yellow and red lines represent the cases of Region A with resolutions of 15 and 30 arcminutes, respectively. Nothing but the resolution of atmospheric pressure is different between the three conditions

of the atmospheric pressure data was much coarser than the offshore bathymetry resolutions in meteotsunami simulations, which were 15 arcseconds or 1 arcminute. This indicates that the resolution of the atmospheric pressure can attribute to the differences in the tsunami amplitude, but the resolution of the offshore bathymetry is more critical.

Next, an evaluation was conducted to identify which offshore regions influenced the amplitude distribution along the coast of Ryukyu Islands. To achieve this, additional numerical experiments were performed using modified bathymetry where ridge areas shallower than a certain threshold depth were masked to a uniform flat depth. The threshold depth was set to 5700 m, which is deeper than the ridge areas but shallower than the Ryukyu Trench and the surrounding deep sea. Two modified bathymetry data were created: one with Daito Ridge and Oki-Daito Ridge masked and the other with Amami Plateau masked. The results were then compared with those of the original simulations.

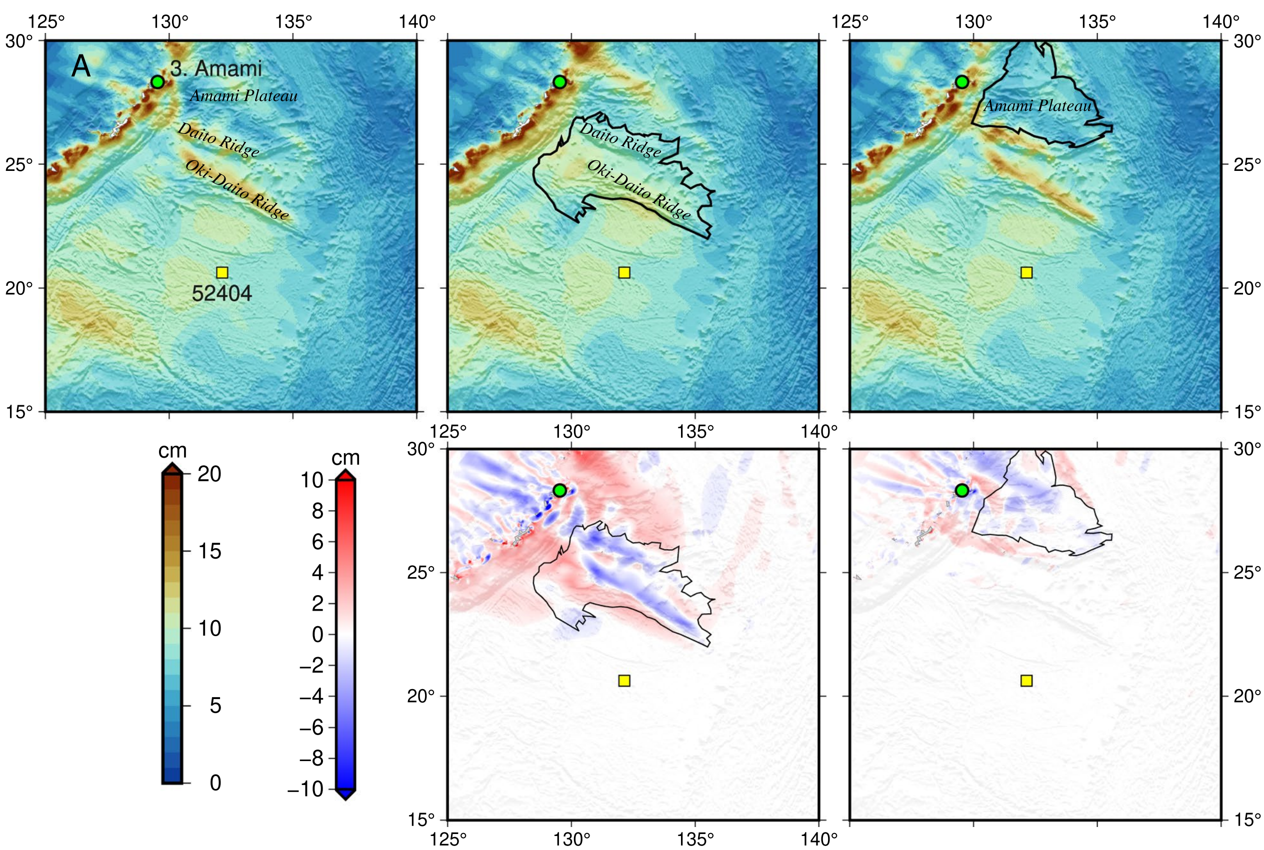

Fig. 11 Spatial distributions of the maximum amplitude off the Ryukyu Islands for the simulation with the masked bathymetry conditions. The top panels show the maximum amplitude, and the bottom panels show the differences of maximum amplitude from the original bathymetry condition. Enclosed areas with black lines in each panel represent the masked regions. The all simulation conditions are the same except for bathymetry conditions. (top-left) The original bathymetry condition, (top-middle) the masked bathymetry around Daito Ridge and Oki-Daito Ridge, (top-right) the masked bathymetry around Amami Plateau, and (bottom) the differences from the original bathymetry condition

Figure 11 shows the spatial distribution of the maximum amplitudes off the Ryukyu Islands for the original and modified simulations. The upper panels show the amplitudes, whereas the lower panels show the differences compared to the original simulation. Enclosed areas with black lines indicate the regions where the bathymetry was modified as flat. The both masked bathymetry simulations significantly altered the spatial distribution of the maximum amplitudes in the downstream areas of the ridges. In particular, in the bathymetry where the Daito Ridge and Oki-Daito Ridge were masked, significant changes in the spatial distribution of amplitudes were observed. Additionally, in the downstream regions of the ridges, the originally localized amplitude distribution tended to become more uniform. This is likely because the shallow depths at the ridges altered the wave propagation direction, creating regions of concentrated and sparse amplitudes downstream. These simulations suggested that the ridges contributed to the wave focusing effects during the event. Furthermore, in the simulations with the modified bathymetry, the amplitudes at 3. Amami were significantly reduced (Fig. S5 in the Supplementary Information).

5 Discussion

The reproduction of this Tonga meteotsunami event in the Ryukyu Island region required a spatial resolution of 15 arcseconds, even in the offshore areas. For typical earthquake tsunamis, such a resolution in deep-sea areas is rarely used, and results that are consistent with observations can be obtained. During the Tonga Event, the representative periods of atmospheric gravity waves are between 10 and 30 min, corresponding to the excited ocean waves (Fig. 3). This period is shorter than tsunamis caused by major earthquakes, making the representation of offshore bathymetry important. Similar waves with characteristic periods are common in meteotsunamis caused by atmospheric disturbances unrelated to volcanic eruptions. Therefore, an accurate prediction of meteotsunamis caused by such atmospheric disturbances would require a similar level of horizontal resolution. As predicting the location and direction of movement of micropressure waves caused by atmospheric disturbances is difficult, high-resolution computations over a wide area are necessary. This implies the necessity of high-load computations for pre-event predictions. It was also confirmed that, in addition to bathymetry resolution, the horizontal resolution of atmospheric pressure contributes to the amplification to a certain extent. This is considered important for forecasting meteotsunamis in the Kyushu region of Japan, where pressure waves from atmospheric disturbances in East China Sea frequently generate meteotsunamis (e.g., Hibiya and Kajiura 1982; Asano et al. 2012; Fukuzawa and Hibiya 2020). Determining the necessary horizontal resolution of atmospheric data for accurate reproduction of meteotsunamis in flat offshore bathymetry will be a crucial focus of future research.

It is important to understand the contributions of the free and forced waves to the amplification of this event. This understanding provides new insights into the future predictability of meteotsunamis. To achieve this goal, an additional numerical experiment was conducted. Atmospheric gravity-wave forcing was terminated when the pressure waves reached the Kyushu-Palau Ridge near 135° E, and the tsunami simulation continued without further pressure forcing. This approach allows the excited waves to propagate as free waves. The results of this simulation are compared with those of previous simulations in which both forced and free waves coexist to evaluate the impact of free waves.

Figure 12a shows a comparison of tsunami waveforms at the Amami station. The blue line at the bottom panel amami is identical to that in Fig. 7, representing the case with atmospheric-pressure forcing, where both forced and free waves coexist. The red line represents the tsunami waveform from the simulation where atmospheric forcing was terminated, indicating that the tsunami waves reaching Amami were free waves. Focusing on the maximum amplitude, the free-wave case shows an amplitude of 51 cm, which is approximately half that in the forced- and free-wave cases, and the observed amplitude. This indicates that a tsunami with an amplitude of a few centimeters offshore near the Kyushu-Palau Ridge could amplify to 50 cm without further atmospheric excitation. The remaining half of the amplification was due to atmospheric forcing from offshore to the coast. Additionally, the experiment with the free-wave case showed a higher attenuation rate after the maximum amplitude, resulting in a shorter tsunami duration compared with the other simulations. The long durations observed at other locations can be attributed to prolonged atmospheric oscillations.

Figure 12a also shows the simulated waveforms at virtual offshore stations where no observational data are available. The locations of these offshore stations are indicated in Fig. 12b. As the waves propagate, differences in phase between the free waves and forced waves become significant, with the shorter frequency components weakening in the cased of free wave only. At Station O2, the forced waves exhibit oscillations with a period of approximately 12 min, occurring five times per hour with an amplitude of 10 cm. In contrast, when only free waves are considered, these oscillations are approximately half in amplitude. Therefore, the components in

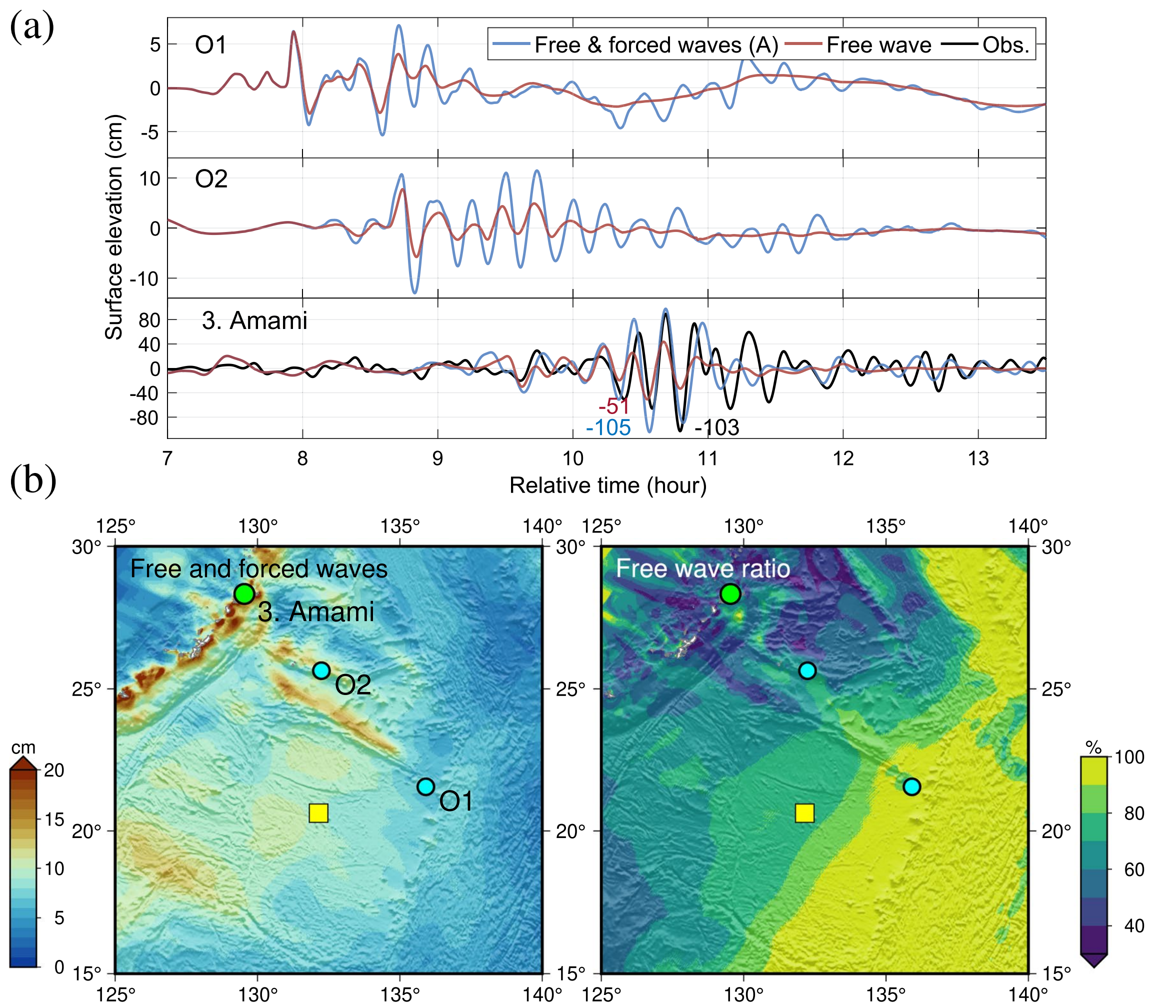

Fig. 12 Comparison of free and forced waves. **a** Waveforms at Amami and virtual two stations off the coast. The locations of offshore stations O1 and O2 are shown in **b**. **b** (left) spatial distribution of the maximum amplitude under the forced and free waves condition and (right) ratio of free wave component to forced and free waves in terms of the maximum amplitude

this frequency band, which are crucial for resonance at Amami, had about half of their amplification contributed by the offshore forced waves.

Figure 12b shows the spatial distribution of the maximum amplitudes from the free-wave simulation and the ratio of these amplitudes to the forced- and free-wave cases. The left panel indicates that free waves are amplified in the ridge regions. Outside these regions, except for the areas where the depth shallowed over the Ryukyu Trench, the tsunami amplitudes attenuated as the waves propagated. As seen in the ratio of the forced and free wave cases (right panel), the ratio decreased monotonically from southeast to northwest outside the ridge regions. However, in the south of Amami Island, the ratio of free waves to the maximum amplitude was high. This suggests that some amplification mechanisms for free waves influenced by the surrounding island topography such as the wave focusing effect exist during and even after passing through the ridges. Additionally, the significant 100-cm amplitude observed can be attributed to continuous atmospheric excitation in shallow coastal areas, combined with these amplification mechanisms, differentiating the region from its surroundings.

Figure 12b shows that the amount of amplification before reaching the coastlines of the Ryukyu Islands from the Ryukyu Trench was significantly different. This difference arises because free waves are primarily amplified by wave shoaling, whereas forced waves receive additional excitation from atmospheric waves. In particular, prolonged weak atmospheric waves have been observed in Japan due to volcanic eruptions (e.g., Nishikawa et al. 2022; Tsukanova and Medvedev 2022). This feature can also contribute to the amplification. For instance, among atmospheric pressure waves with multiple wave speeds, assume that the faster waves excite the sea surface. When the resulting tsunami propagates up a slope and its speed decreases, the slower atmospheric pressure waves catch up with the tsunami, leading to further amplification (Kakinuma and Kosugi 2024). Additionally, the ratio of forced waves to free waves depends on the propagation direction of the pressure waves, the slope of the continental shelf, and the number of successive waves (Tonegawa and Fukao 2022; Ho et al. 2023). For future prediction and risk assessment of meteotsunamis, it is important to understand the conditions under which successive waves of certain wavelengths result in significant meteotsunamis in each region.

6 Conclusions

In this study, we conducted numerical simulations of the meteotsunami generated by the 2022 Tonga volcanic eruption, which has been observed worldwide. The target area was the Ryukyu Islands in Japan, where a maximum amplitude of 100 cm was recorded. Two types of models were used to simulate the pressure waves from the volcanic eruptions: one based on the superposition of single waves tuned using the dispersion relation of atmospheric gravity waves (synthetic waves), and the second based on a detailed numerical model that assumed the release of a heat source from the eruption vent. Simulations using synthetic pressure waves showed good agreement with the observations, including an amplitude exceeding 100 cm at the Amami location.

Next, to analyze the factors contributing to the large amplitude observed at Amami, numerical experiments were conducted with deliberately limited resolution in offshore areas deeper than 2000 m while maintaining high resolution in coastal bathymetry. When the simulations were run under otherwise identical conditions, the amplitude along the Amami Coast decreased from approximately 100 cm to 60 cm. This indicates that the offshore microtopography significantly contributes to coastal amplification. In particular, the difference in amplitude due to resolution was notable in ridge areas with depths ranging from 2000 to 5000 m. Even in the simulation where only the horizontal resolution of the atmospheric data was coarsened while maintaining the same fine bathymetry, nearly the same amplitude was obtained at Amami. This experiment highlighted the importance not only of capturing the pressure waves but also of sufficiently resolving the bathymetry.

Finally, the proportion of free waves to the total pressure amplitude was quantified by setting the atmospheric pressure amplitude to zero after atmospheric gravity waves passed over the offshore ridges of the Ryukyu Islands, thereby eliminating the generation of forced waves. Even at offshore amplitudes of less than 5 cm, free waves alone could amplify to 50 cm at Amami, which is approximately half the amplitude when forced waves are also considered. These results provide crucial insights into assessing the future predictability of meteotsunamis. Future research should investigate the necessary resolution and relationship between the wavelength and speed of atmospheric waves for accurate predictions of meteotsunamis, including those caused by atmospheric disturbances and not just volcanic eruptions. This will further enhance our understanding of the amplification phenomena in meteotsunamis.

Supplementary Information

The online version contains supplementary material available at https://doi.org/10.1186/s40623-025-02148-2.

Supplementary Material 1.

Acknowledgements

The JAGUAR simulation was conducted using the Earth Simulator at JAMSTEC. The authors acknowledge the Japan Meteorological Agency for providing the atmospheric pressure and tidal observation records.

Author contributions

TM conducted the study, curated the data, performed the numerical simulations, and set the optimized numerical conditions. TM and AN tuned the parameters and summarized the results. WS performed numerical simulations of the atmosphere and processed the simulated data. TY, NM, and TS designed numerical experiments and supervised the study. TCH processed and analyzed the observed data. TM wrote the manuscript. All authors discussed the results and critically reviewed and approved the final version of the manuscript.

Funding

This study was supported by JSPS KAKENHI Grant Number JP23K13413 and Core-to-Core Collaborative Research Program of Earthquake Research Institute, The University of Tokyo, and Disaster Prevention Research Institute, Kyoto University (2024-K-01). TM, SW, TY, NM, and TS were supported by MEXT-Program for the advanced studies of climate change projection (SENTAN) Grant Numbers JPMXD0722681344 and JPMXD0722678534. SW was supported by JSPS KAKENHI Grant Number JP24K00706.

Availability of data and materials

The spatio-temporal data of the synthetic pressure waves in this study are available at Zenodo. (https://doi.org/10.5281/zenodo.7839906). The setup files of the GeoClaw simulation are available at Zenodo. (https://zenodo.org/doi/10.5281/zenodo.12802556). Bathymetry data provided by the Central Disaster Management Council, Cabinet Office of Japan, are available at https://www.bousai.go.jp. GEBCO Gridded Bathymetry data are available at https://download.gebco.net. Ocean bottom pressure data (DART) from National Oceanic and Atmospheric Administration are available at https://doi.org/10.7289/V5F18WNS. The latest accession to all URLs was January 2025.

Declarations

Competing interests

The authors declare no competing interests.

Author details
[1]Disaster Prevention Research Institute, Kyoto University, Gokasho, Uji, Kyoto 611-0011, Japan. [2]Graduate School of Science and Engineering, Kansai University, Osaka, Japan. [3]Research Institute of Global Change (RIGC) and WPI-AIMEC, Japan Agency for Marine-Earth Science and Technology (JAMSTEC), Kanagawa, Japan. [4]Faculty of Environmental and Urban Engineering, Kansai University, Osaka, Japan. [5]School of Engineering, Swansea University, Swansea, UK. [6]Center for Computational Science, RIKEN, Hyogo, Japan.

Received: 5 August 2024 Accepted: 3 February 2025
Published online: 24 February 2025

References

Asano T, Yamashiro T, Nishimura N (2012) Field observations of meteotsunami locally called "Abiki" in Urauchi bay, Kami-Koshiki Island, Japan. Nat Hazards 64(2):1685–1706. https://doi.org/10.1007/s11069-012-0330-2

Carvajal M, Sepúlveda I, Gubler A, Garreaud R (2022) Worldwide signature of the 2022 Tonga volcanic Tsunami. Geophys Res Lett 49(6):8–11. https://doi.org/10.1029/2022GL098153

Devlin AT, Jay DA, Talke SA, Pan J (2023) Global water level variability observed after the Hunga Tonga-Hunga Ha'apai volcanic Tsunami of 2022. Ocean Sci 19:517–534. https://doi.org/10.5194/os-19-517-2023

Fukuzawa K, Hibiya T (2020) The amplification mechanism of a meteo-tsunami originating off the western coast of Kyushu Island of Japan in the winter of 2010. J Oceanogr 76(3):169–182. https://doi.org/10.1007/s10872-019-00536-3

Heinrich P, Gailler A, Dupont A, Rey V, Hébert H, Listowski C (2023) Observations and simulations of the meteotsunami generated by the Tonga eruption on 15 January 2022 in the Mediterranean Sea. Geophys J Int 234:903–914. https://doi.org/10.1093/gji/ggad092

Hibiya T, Kajiura K (1982) Origin of the Abiki phenomenon (a kind of seiche) in Nagasaki bay. J Oceanogr Soc Japan 38(3):172–182. https://doi.org/10.1007/BF02110288

Ho TC, Mori N, Yamada M (2023) Ocean gravity waves generated by the meteotsunami at the Japan Trench following the 2022 Tonga volcanic eruption. Earth Planets Space 75(1):25. https://doi.org/10.1186/s40623-023-01775-x

Horvath A, Vadas SL, Stephan CC, Buehler SA (2024) One-minute resolution GOES-R observations of Lamb and gravity waves triggered by the Hunga Tonga-Hunga Ha'apai eruptions on 15 January 2022. J Geophys Res Atmos. https://doi.org/10.1029/2023JD039329

Imamura F, Suppasri A, Arikawa T, Koshimura S, Satake K, Tanioka Y (2022) Preliminary observations and impact in Japan of the tsunami caused by the Tonga volcanic eruption on January 15, 2022. Pure Appl Geophys 179:1549–1560. https://doi.org/10.1007/s00024-022-03058-0

Kakinuma T, Kosugi J (2024) Numerical study on the excitation and propagation of surface/internal waves due to air pressure waves over topography. Water Waves. https://doi.org/10.1007/s42286-024-00099-x

Kawase K (2013) Concise derivation of extensive coordinate conversion formulae in the Gauss-Krüger projection. Bull Geospat Inf Authority Japan 60:1–6

Kubo H, Kubota T, Suzuki W, Aoi S, Sandanbata O, Chikasada N, Ueda H (2022) Ocean-wave phenomenon around Japan due to the 2022 Tonga eruption observed by the wide and dense ocean-bottom pressure gauge networks. Earth Planets Space 74:104. https://doi.org/10.1186/s40623-022-01663-w

Kubota T, Saito T, Nishida K (2022) Global fast-traveling tsunamis driven by atmospheric Lamb waves on the 2022 Tonga eruption. Science 377(6601):91–94. https://doi.org/10.1126/science.abo4364

Lynett P, McCann M, Zhou Z, Renteria W, Borrero J, Greer D, Fa'anunu O, Bosserelle C, Jaffe B, La Selle S, Ritchie A, Snyder A, Nasr B, Bott J, Graehl N, Synolakis C, Ebrahimi B, Cinar GE (2022) Diverse tsunamigenesis triggered by the Hunga Tonga-Hunga Ha'apai eruption. Nature 609(7928):728–733. https://doi.org/10.1038/s41586-022-05170-6

Mandli KT, Dawson CN (2014) Adaptive mesh refinement for storm surge. Ocean Model 75:36–50. https://doi.org/10.1016/j.ocemod.2014.01.002

Matoza RS, Fee D, Assink JD, Iezzi AM, Green DN, Kim K, Toney L, Lecocq T, Krishnamoorthy S, Lalande JM, Kiwamu Gee KL, Haney MM, Ortiz HD, Brissaud Q, Martire L, Rolland L, Vergados P, Nippress A, Park J, Shani-Kadmiel S, Witsil A, Arrowsmith S, Caudron C, Watada S, Perttu AB, Taisne B, Mialle P, Pichon AL, Vergoz J, Hupe P, Blom PS, Waxler R, Angelis SD, Snively JB, Ringler AT, Anthony RE, Jolly AD, Kilgour G, Averbuch G, Ripepe M, Ichihara M, Arciniega-Ceballos A, Astafyeva E, Ceranna L, Cevuard S, Che IY, Negri RD, Ebeling CW, Evers LG, Franco-Marin LE, Gabrielson TB, Hafner K, Harrison RG, Komjathy A, Lacanna G, Lyons J, Macpherson KA, Marchetti E, McKee KF, Mellors RJ, Mendo-Pérez G, Mikesell TD, Munaibari E, Oyola-Merced M, Park I, Pilger C, Ramos C, Ruiz MC, Sabatini R, Schwaiger HF, Tailpied D, Talmadge C, Vidot J, Webster J, Wilson DC (2022) Atmospheric waves and global seismoacoustic observations of the January 2022 Hunga eruption, Tonga. Science 377(6601):95–100. https://doi.org/10.1126/science.abo7063

Miyashita T, Nishino A, Ho TC, Yasuda T, Mori N, Shimura T, Fukui N (2023) Multi-scale simulation of subsequent tsunami waves in Japan excited by air pressure waves due to the 2022 Tonga volcanic eruption. Pure Appl Geophys 180:3195–3223. https://doi.org/10.1007/s00024-023-03332-9

Monserrat S, Vilibić I, Rabinovich AB (2006) Meteotsunamis: atmospherically induced destructive ocean waves in the tsunami frequency band. Nat Hazards Earth Syst Sci 6(6):1035–1051. https://doi.org/10.5194/nhess-6-1035-2006

Mungov G, Eblé M, Bouchard R (2013) DART tsunameter retrospective and real-time data: a reflection on 10 years of processing in support of tsunami research and operations. Pure Appl Geophys 170:1369–1384. https://doi.org/10.1007/s00024-012-0477-5

Nishikawa Y, Yamamoto M, Nakajima K, Hamama I, Saito H, Kakinami Y, Yamada M, Ho TC (2022) Observation and simulation of atmospheric gravity waves exciting subsequent tsunami along the coastline of Japan after Tonga explosion event. Sci Rep 12(1):22354. https://doi.org/10.1038/s41598-022-25854-3

Nomanbhoy N, Satake K (1995) Generation mechanism of tsunamis from the 1883 Krakatau eruption. Geophys Res Lett 22(4):509–512. https://doi.org/10.1029/94GL03219

Omira R, Ramalho RS, Kim J, González PJ, Kadri U, Miranda JM, Carrilho F, Baptista MA (2022) Global Tonga tsunami explained by a fast-moving atmospheric source. Nature 609(7928):734–740. https://doi.org/10.1038/s41586-022-04926-4

Pacheco EE, Velasquez JP, Flores R, Condori L, Fajardo G, Kuyeng K, Scipion DE, Milla M, Conte JF, Poblet FL, Chau JL, Suclupe J, Rojas R, Manay E (2024) The impact of the Hunga Tonga-Hunga Ha'apai volcanic eruption on the Peruvian atmosphere: from the sea surface to the ionosphere. Earth Planets Space 76:79. https://doi.org/10.1186/s40623-024-02022-7

Pakoksung K, Suppasri A, Imamura F (2023) Resonance characteristics of tsunami in bay of Japan by the Hunga Tonga-Hunga Haápai volcano eruption on 15th January 2022. Sci Rep 13:18385. https://doi.org/10.1038/s41598-023-45601-6

Rabinovich AB (2020) Twenty-seven years of progress in the science of meteorological tsunamis following the 1992 Daytona beach event. Pure Appl Geophys 177(3):1193–1230. https://doi.org/10.1007/s00024-019-02349-3

Shinbori A, Otsuka Y, Sori T, Nishioka M, Septi P, Tsuda T, Nishitani N, Kumamoto A, Tsuchiya F, Matsuda S, Kasahara Y, Matsuoka A, Nakamura S, Miyoshi Y, Shinohara I (2023) New aspects of the upper atmospheric disturbances caused by the explosive eruption of the 2022 Hunga Tonga-Hunga Ha'apai volcano. Earth Planets Space 75:175. https://doi.org/10.1186/s40623-023-01930-4

Suzuki T, Nakano M, Watanabe S, Tatebe H, Takano Y (2023) Mechanism of a meteorological tsunami reaching the Japanese coast caused by Lamb and Pekeris waves generated by the 2022 Tonga eruption. Ocean Model 181:102153. https://doi.org/10.1016/j.ocemod.2022.102153

Takahashi H, Figueiredo CA, Barros D, Wrasse CM, Giongo GA, Honda RH, Vital LF, Resende LC, Nyassor PK, Ayorinde TT, Carmo CS, Padua MB, Otsuka Y (2023) Ionospheric disturbances over South America related to Tonga volcanic eruption. Earth Planets Space. https://doi.org/10.1186/s40623-023-01844-1

Tanioka Y, Yamanaka Y, Nakagaki T (2022) Characteristics of the deep sea tsunami excited offshore Japan due to the air wave from the 2022 Tonga eruption. Earth Planets Space 74(1):61. https://doi.org/10.1186/s40623-022-01614-5

Tonegawa T, Fukao Y (2022) Wave propagation of meteotsunamis and generation of free tsunamis in the sloping area of the japan trench for the

2022 hunga-tonga volcanic eruption. Earth Planets Space 74:159. https://doi.org/10.1186/s40623-022-01727-x
Tsukanova E, Medvedev I (2022) The observations of the 2022 Tonga-Hunga tsunami waves in the Sea of Japan. Pure Appl Geophys 179(12):4279–4299. https://doi.org/10.1007/s00024-022-03191-w
Wang Y, Imai K, Miyashita T, Ariyoshi K, Takahashi N, Satake K (2023) Coastal tsunami prediction in Tohoku region, Japan, based on S-net observations using artificial neural network. Earth Planets Space 75:154. https://doi.org/10.1186/s40623-023-01912-6
Watanabe S, Miyahara S (2009) Quantification of the gravity wave forcing of the migrating diurnal tide in a gravity wave-resolving general circulation model. J Geophys Res Atmos. https://doi.org/10.1029/2008JD011218
Watanabe S, Hamilton K, Sakazaki T, Nakano M (2022) First detection of the Pekeris internal global atmospheric resonance: evidence from the 2022 Tonga eruption and from global reanalysis data. J Atmos Sci 79(11):3027–3043. https://doi.org/10.1175/JAS-D-22-0078.1
Wright CJ, Hindley NP, Alexander MJ, Barlow M, Hoffmann L, Mitchell CN, Prata F, Bouillon M, Carstens J, Clerbaux C, Osprey SM, Powell N, Randall CE, Yue J (2022) Surface-to-space atmospheric waves from Hunga Tonga-Hunga Ha'apai eruption. Nature 609(7928):741–746. https://doi.org/10.1038/s41586-022-05012-5
Yamada M, Ho TC, Mori J, Nishikawa Y, Yamamoto MY (2022) Tsunami triggered by the Lamb wave from the 2022 Tonga volcanic eruption and transition in the offshore Japan region. Geophys Res Lett 49(15):1–9. https://doi.org/10.1029/2022GL098752
Yuen DA, Scruggs MA, Spera FJ, Zheng Y, Hu H, McNutt SR, Thompson G, Mandli K, Keller BR, Wei SS, Peng Z, Zhou Z, Mulargia F, Tanioka Y (2022) Under the surface: pressure-induced planetary-scale waves, volcanic lightning, and gaseous clouds caused by the submarine eruption of Hunga Tonga-Hunga Ha'apai volcano. Earthquake Res Adv 2(3):100134. https://doi.org/10.1016/j.eqrea.2022.100134
Zaytsev O, Rabinovich AB, Thomson RE (2024) The 2022 Tonga tsunami on the Pacific and Atlantic coasts of the Americas. J Geophys Res Oceans. https://doi.org/10.1029/2024JC020926

Publisher's Note